Torsional fatigue mechanisms of an A357-T6 cast aluminium alloy

I. Serrano-Munoz, D. Shiozawa, Sylvain Dancette, C. Verdu, J.-Y. Buffiere

Version of Record: https://www.sciencedirect.com/science/article/pii/S1359645420307400
Manuscript_51fb397c50f98d74d2390b6d903a7787

Torsional fatigue mechanisms of an A357-T6 cast aluminium alloy

I. Serrano-Munoz[a,b,*], D. Shiozawa[c], S. Dancette[a], C. Verdu[a], J.-Y. Buffiere[a,*]

[a] *Université de Lyon, INSA-Lyon, MATEIS CNRS UMR 5510, Villeurbanne 69621 Cedex, France*
[b] *Current address: Bundesanstalt für Materialforschung und –prüfung (BAM), Unter den Eichen 87, 12205 Berlin, Germany*
[c] *Department of Mechanical Engineering, Kobe University, 1-1, Rokkodai, Nada, Kobe 657-8501, Japan*

Abstract

The mechanisms controlling the fatigue response of an A357-T6 cast aluminium alloy under cyclic torsional loading are investigated. Surface crack monitoring coupled with Electron BackScattering Diffraction (EBSD) analysis is used to study crack initiation. Determination of S-N curve combined with interrupted in situ fatigue testing using synchrotron tomography allows the study of the propagation behaviour. It is observed that fractographic morphologies depend on the stress level. At intermediate-low stress level (τ_{max} < 100 MPa) the crystallography controls crack initiation and propagation periods. Cracks are usually nucleated in mode II from slip planes close to the specimen axis or perpendicular to it. Mode II crack growth dominates the early stages of crack propagation as mode III inward crack growth is rapidly decelerated. This behaviour leads to the formation of characteristic shallow cracks. Once the crack is long enough for the mode II driving force to be overtaken by mode III, propagation branches into ~45° mode I.

Keywords: A357-T6 casting, fractographic observations, EBSD analysis, X-ray synchrotron tomography, torsional in situ fatigue testing, SIF evaluation

1. Introduction

Al-Si cast alloys are attractive solutions for the production of light components with complex shapes. However, a pronounced fatigue response variability [1–10], specially in the High Cycle Fatigue (HCF, $10^5 < N_f < 10^7$ cycles) regime, limits their use. Critical parts are restricted to assembled wrought Al solutions, a comparatively cost-intensive process. Potential advances towards a larger use of Al-Si castings require further understanding of the microstructure-performance relations under complex loading scenarios.

The total fatigue life of a specimen (N_T) can be written as:

$$N_T = N_i + N_p \tag{1}$$

*Corresponding authors:
Email addresses: itziar.serrano.munoz@gmail.com (I. Serrano-Munoz), jean-yves.buffiere@insa-lyon.fr (J.-Y. Buffiere)

where the initiation period (N_i) corresponds to the development of cracks longer than intrinsic microstructural features such as grains or phases. The propagation period (N_p) is the number of cycles spent in crack propagation until the final failure [11]. Under pure tensile loading, cracks exhibit a crystallographic mode II propagation at 45° during N_i, evolving to perpendicular (with respect to the loading direction) mode I propagation during N_p. Usually, a single crack dominates the propagation period until final failure occurs.

Because in pure torsion the stress value is maximum at the free surface and decreases towards the interior, torsion crack initiation is always a surface phenomenon. As illustrated in Fig. 2a, cracks propagate in mode II along the surface and in mode III towards the interior, leading to a mixed mode II-mode III propagation. When the crack-tip driving force is high enough, mode III is thought to dominate producing macroscopically 90° flat fracture surfaces [12–14]. For intermediate stress levels, the mode II-mode III (hereafter simply named mode II) propagation is eventually arrested by a crack-closing effect. At this point, mode I stress intensity values overtake mode III ones and crack growth switches into 45° mode I propagation. This leads to macroscopic 45° spiral-like fracture surfaces when using smooth specimens [15]. Contrary to tensile testing, torsion leads to multi-cracking phenomena where several cracks can propagate simultaneously.

Another important difference between tension and torsion is the extent of N_i. Under tension loading, this period can account up to ~90% of the total fatigue life, although it can be severely reduced (or even suppressed) when surface/subsurface casting defects are present [1–10]. On the other hand, much lower values of N_i have been reported in torsion; for instance, N_i was found to be 10% of the total fatigue life in the case of an Inconel 718 material [16].

Regarding the torsional behaviour of Al-Si castings, it has been recently observed [17] that the influence of surface/subsurface casting defects is, in general, considerably less deleterious to the total fatigue life. For defect-free specimens[1], Secondary Dendrite Arm Spacing (SDAS) is the parameter controlling the fatigue limit [18]. The effect of SDAS is much more pronounced under torsion cycling, with higher SDAS values leading to lower fatigue limits. Multi-crack initiation has been reported occurring at eutectic silicon particles, on planes of maximal shear stress (0° and/or 90°) [19]. Crack propagation (using smooth specimens) produces tortuous fracture surfaces where mode III (on both 0° and 90°planes) is dominant [20]. Final failure generally occurs by linkage of cracks that are simultaneously propagating in ~45° mode I. Compared to the available literature on uniaxial fatigue, the torsional fatigue mechanism of Al-Si casting have received much less attention. One reason for this is the inwards evolution of cracks, which means that the damage mechanisms cannot be only understood by monitoring the surface of specimens and need to be inferred from post-mortem examinations of complex fracture surfaces, where the rubbing between crack surfaces usually smears the propagation features.

[1] In this study, defect-free specimens are considered as those containing no life-limiting porosity or oxides at the surface/subsurface.

The present work is focused on the torsional fatigue behaviour of an A357-T6 material. Optical surface crack monitoring combined with Electron BackScattering Diffraction (EBSD) analysis was used to investigate the initiation period. Fractographic post-mortem examinations gave insight of the general crack propagation mechanisms, while the chronology of crack growth below the surface was specifically studied using in situ testing synchrotron tomography. The results are used to examine the influence of microstructural parameters on the torsional response of the studied cast alloy.

2. Material and experimental methods

2.1. Material

The A357-T6 cast aluminium alloy examined in this study had a nominal composition of (by wt. pct.) 6.94 Si, 0.56 Mg, 0.097 Fe, 0.13 Ti, <0.015 Cu, <0.03 Mn, <0.003 Pb and balance Al. The Secondary Dendrite Arm Spacing (SDAS) is 38 ±6 μm and the average grain size is $\varnothing_{eq}$ = 500 μm (area-weighted average). These parameters were evaluated at the centre of the rods. The pore size was evaluated using laboratory X ray tomography (voxel size = 12 μm) on seven cylindrical specimens ($\varnothing$6 mm, height = 25 mm). The size of each pore is defined as the diameter $\varnothing_{eq}^{XRT} = (\frac{6\times Volume}{\pi})^{\frac{1}{3}}$ of a sphere having the same volume as the measured pore. The average pore size is $\varnothing_{eq}^{XRT}$ = 42 μm±15 μm. The pore volume fraction is 0.002%.

As-cast $\varnothing$30x250 mm rods were subjected to a T6 peak-ageing heat treatment, consisting of solution heat treatment at 540 °C for 10 h in an air circulated furnace, subsequently followed by water quenching at room temperature and artificially ageing at 160 °C for 8 h. The Young's modulus is 73.5 GPa, the ultimate tensile strength σ_{UTS} = 335 MPa and the yield strength σ_{YS} = 275 MPa. More details about the material properties can be found in reference [21].

2.2. Fatigue testing

Depending on the mechanisms to be studied, two different types of specimen geometries were required.

2.2.1. Macroscopic specimens

The S-N fully reversed (R=-1) torsional experiments were carried out using a MTS 809 Axial/Torsional servo-hydraulic machine running at 10 Hz in room temperature air. Torsion fatigue specimens were designed in order to comply with the ISO-1352 Standard [22]. The geometry is shown in Fig. 1a. Two fatigue specimens per rod were machined out, with the specimen gauge corresponding to the rod centre. In order to eliminate any machining traces and ensure consistent surface finish, the $\varnothing$6 mm gauges were manually polished along the longitudinal direction using 4000 grit SiC papers. Post-mortem specimens were used to perform fracture surface examination.

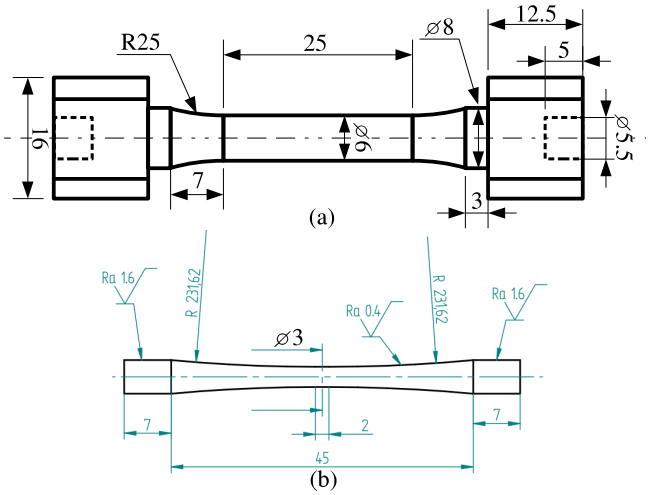

Figure 1: (a) Geometry of the macroscopic torsion specimens. Dimensions are in millimetres. (b) Geometry of the tomography specimens.

2.2.2. Tomography specimens

The geometry used for the tomography specimens is shown in Fig. 1b. This geometry is a size compromise between a volume large enough to observe the multi-cracking phenomenon and obtaining sufficient resolution for crack imaging. Contrary to the macroscopic ones, the tomography specimens were carved out using electrical discharge machining (EDM) from regions close to the rod free surface (*i.e.,* close to the 30 mm perimeter). Longitudinal manual polishing with 2400 and 4000 grit SiC papers was subsequently performed.

The tomography experiments were carried out at ID19 (ESRF [23]) using a dedicated in situ torsion machine (developed at INSA Lyon) working at 10 Hz and R = -1. A pink beam of 25 keV was used for scans with 1800 projections over 180° at 1 s per projection. A FreLoN 2K14 ccd camera was mounted on a visible light microscope coupled to a LSO 8.8 µm scintillator. The propagation distance was ~80 mm. A voxel size of 3.5 μm allowed the monitoring of a ⌀3×7 mm^3 volume. In order to optimize the use of beamtime, the fatigue specimens were pre-cracked in the laboratory, using Scanning Electron Microscopy (SEM) for surface crack monitoring. During the synchrotron in situ testing, scans were recorded every 10,000 cycles. The Fiji™ [24] free-software was used for the visualisation and segmentation of the cracks; the crack area projected along the longitudinal axis was used for the measurement of crack growth.

2.3. Surface crack monitoring

A flattened zone (~3 mm width by 10 mm length) was ground off in one of the macroscopic specimens in order to perform surface crack monitoring using optical microscopy. The flattened zone was manually polished using 2500 and 4000 grit SiC papers and 3 μm oil-based diamond suspensions. The final polishing required a smooth chemo-

mechanical polishing using colloidal silica (0.02 μm) for 2.5 minutes. The horizontal projection of the crack length was used for the measurement of crack growth.

2.3.1. EBSD analysis and computation of the slip activity

Once the surface monitoring is concluded, the fatigue specimen is sectioned in order to reduce the size and isolate the gauge. A ZEISS SUPRA VP55 SEM equipped with a NordlysF+ camera (Oxford Instruments) was used for the EBSD analysis (operated at 20 KeV and a working distance of 13 mm). The AZtecHKL™ software (also Oxford Instruments) was used for pattern indexing and data collection [25]. The spatial resolution of the EBSD maps is 5μm x 5 μm per pixel.The EBSD results are used to investigate the slip activity ($\dot{\gamma}^s$) of each potential slip system in the investigated grains. The Taylor model [26–29] assumes iso-deformation of all grains. Such simple assumption is known as a reliable starting point for the analysis of plasticity and texture [26, 29], yet violating equilibrium of stress at the grain boundaries. The FORTRAN routine performing the calculation is described in detail in references [27, 30, 31]. The calculation was ran assuming plane stress, which is motivated by the free surface analysed by EBSD. A small uniform shear of 1% was applied in order to mimic the torsion deformation state at the gauge surface during the fatigue experiment. The shear rate $\dot{\gamma}^s$ on each system s, among the twelve FCC $\{111\}\langle 110\rangle$ slip systems, was calculated as a power law depending on the resolved shear stress τ^s:

$$\dot{\gamma}^s = \dot{\gamma}_0 \left| \frac{\tau^s}{\tau_c} \right|^{1/m} \mathrm{sign}(\tau^s) \tag{2}$$

where $\dot{\gamma}_0 = 0.001$ is the reference slip rate, $m = 0.025$ is the strain-rate sensitivity exponent and $\tau_c = 100\,\mathrm{MPa}$ is the critical resolved shear stress. This set of parameters was chosen to guarantee that the onset of plasticity occurs at a stress level corresponding to the material yield strength level, with a low strain-rate sensitivity. The Taylor factor M measures the amount of slip required in a given crystal to achieve the prescribed equivalent plastic strain rate D^p_{eq}:

$$M = \frac{\sum_s |\dot{\gamma}^s|}{D^p_{eq}} \tag{3}$$

With the computed stress state $\boldsymbol{\sigma}$ and slip rates in the grains, it is then straightforward to compute the traces of the most activated slip systems at the specimen surface. The EBSD map with the colouring corresponding to the Taylor factor of each grain was plotted using MTEX Toolbox [32].

3. Results

3.1. S-N curves and fractographic observations

Fig. 2b shows, in red, the fully reversed torsional S-N curve. The tension-compression S-N curve is added in black for comparison purposes [21]. It is observed that the fatigue life variability is less pronounced in torsion. The two curves tend to converge at 10^7 cycles giving a fatigue limit ratio of $\tau_f/\sigma_f = 0.95$. This is in good agreement with literature results, which report fatigue limit ratios close to 1 for cast materials [15].

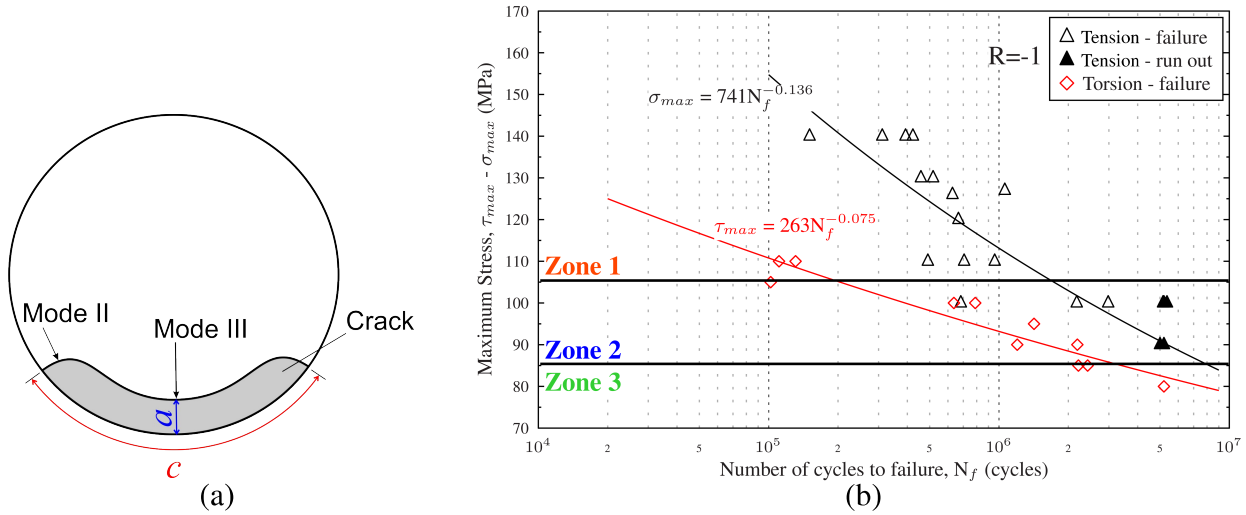

Figure 2: (a) Schematic illustration of a torsional crack propagating in mode II along the free surface and in mode III towards the interior. (b) Fully reversed torsion (in red) and tension-compression (in black) S-N curves. The two horizontal lines indicate the limits of the three fractographic zones.

Depending on the stress level, three distinct fractographic zones have been observed and are summarised schematically in Fig. 3. Zone 1 corresponds to the highest stresses ($\tau_{max} > 105$ MPa, Fig. 3a). This zone is characteristic of the 0° flat fracture surfaces which exhibit crystallographic initiation sites where some thin layers of debris are usually formed. Some circumferential patterns resulting from mode III rubbing can be observed in the crack propagation region. Final failure produces regions with ductile dimples.

The intermediate stress levels (105 MPa > τ_{max} > 85 MPa, Fig. 3b) of Zone 2 produce fracture surfaces with tortuous morphologies. Some thick layers of debris partially cover the crystallographic initiation sites. The propagation is chaotic as cracks seems to indistinctly evolve in 0° mode II, 90° mode II or 45° mode I. Final failure occurs by linkage of simultaneously propagating cracks. Interestingly, some mode I propagation striations can be observed on some of the fracture surfaces.

Spiral-like fracture surfaces correspond to Zone 3 (low stress levels, $\tau_{max} < 85$ MPa, Fig. 3c). The crystallographic initiation sites also exhibit thick murky debris. The entire crack propagation occurs in macroscopic 45° mode I.

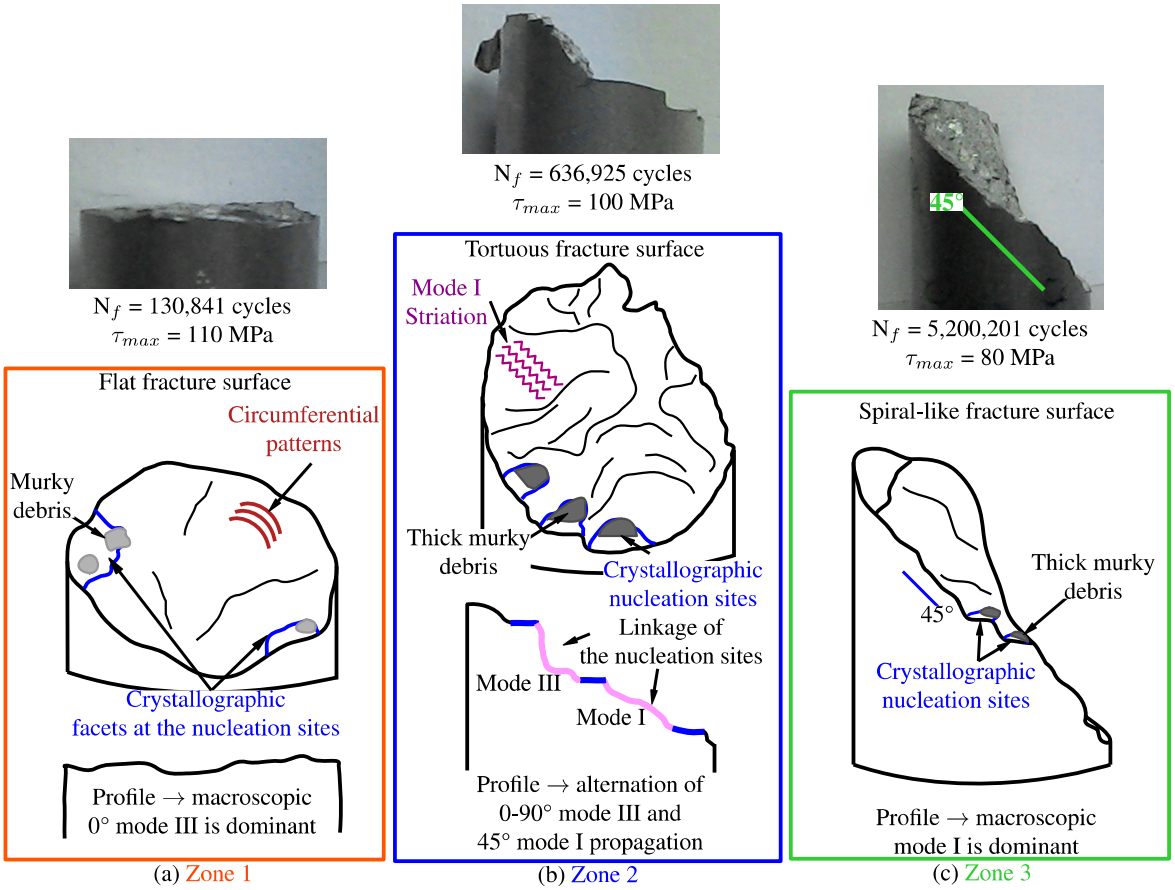

Figure 3: Profile image and schematic illustration of fractures surfaces showing the principal features observed during SEM examination for (a) Zone 1, (b) Zone 2, and (c) Zone 3.

Note that the initiation sites of all examined specimens are pore free. This lack of pore induced initiation is in good agreement with the diminished deleterious effect of casting defects reported in [17].

3.2. Surface crack initiation

It was decided to perform crack monitoring at τ_{max} = 95 MPa because the multi-cracking nature of torsional cycling is more pronounced in this region of the fatigue curve. Four different cracks were detected during the experiment. Fig. 4a,b shows the chronology observed for Crack 1. After 200,000 cycles, the crack had already propagated 753 μm and after 40,000 cycles more, it already exhibited deflections on both left and right sides to reach a total length of 1,360 μm. Propagation on the left of Fig. 4b continued in mode II but on the right side the crack switched to mode I. The experiment was concluded at this point to perform EBSD analysis.

Fig. 4c shows the IPF-Z map where the four cracks are shown using black lines. Crack 1 is thought to have nucleated in two different grains and continued propagation with similar crystallographic orientation, even when growing through some neighbouring grains. Crack 2 nucleated in the relatively smaller Grain 5 and was deflected

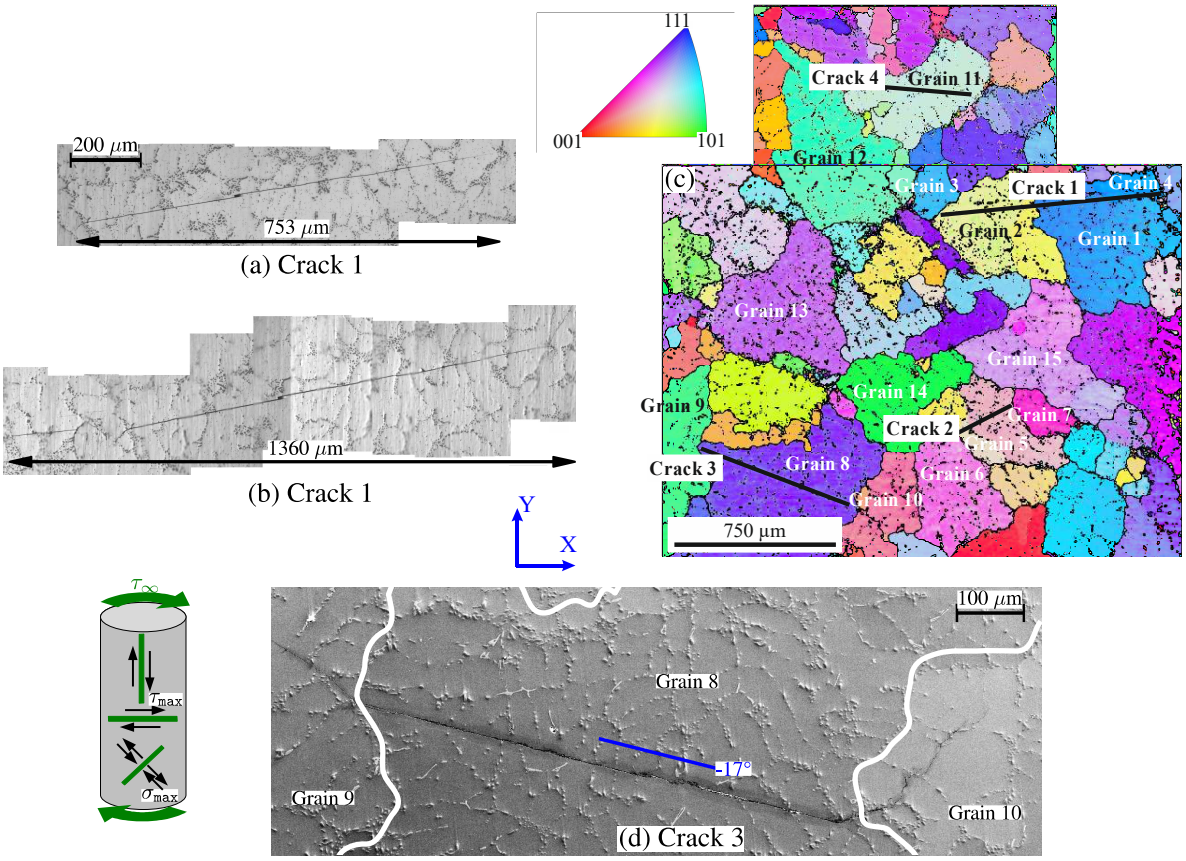

Figure 4: Surface monitoring of crack initiation at τ_{max} = 95 MPa: (a) Image of Crack 1 after 200,000 cycles; (b) Image of Crack 1 after 240,000 cycles when the experiment was concluded. (c) EBSD IPF-Z map showing the four cracks initiated during the monitoring. The crystallographic orientations of cracks are shown in black. (d) SEM image at low magnification of Crack 3 with grain boundaries outlined in white. The crack propagation angles were measured with respect to the horizontal direction of the image.

when entering the neighbouring Grain 6 and Grain 7. Crack 3 nucleated within a large grain (Grain 8) and switched into mode I to continue propagation within Grain 10 and Grain 9 (Fig. 4d). Finally, a fourth grain (Grain 11) nucleated a crystallographic crack. Note that none of the observed cracks nucleated exactly at 0° where the shear stress is maximal. Hereafter, the initiation period of the studied material is referred to as the number of cycles necessary to nucleate and propagate a crack until it fully enters into the neighbouring grains. At τ_{max} = 95 MPa, the initiation period accounts for 30% of the expected fatigue life (see Fig. 2b).

3.3. Crack propagation

3.3.1. Synchrotron in situ fatigue testing

The cycling was performed at a relatively high stress level (τ_{max} = 125 MPa). Four cracks are already present (see Fig. 5a) within the field of view (fov) when the pre-cracked specimen is first scanned after 195,000 cycles. Crack 11 and Crack 12 propagated in mode II at planes close to 0° while Crack 13 and Crack 14 nucleated at ~90° planes. The

black arrow indicates the beginning of mode I crack branch. Fig. 5b shows the 3D spatial arrangement of the four cracks at 215,000 cycles. Hereafter, focus is made on the propagation of the largest crack (Crack 12).

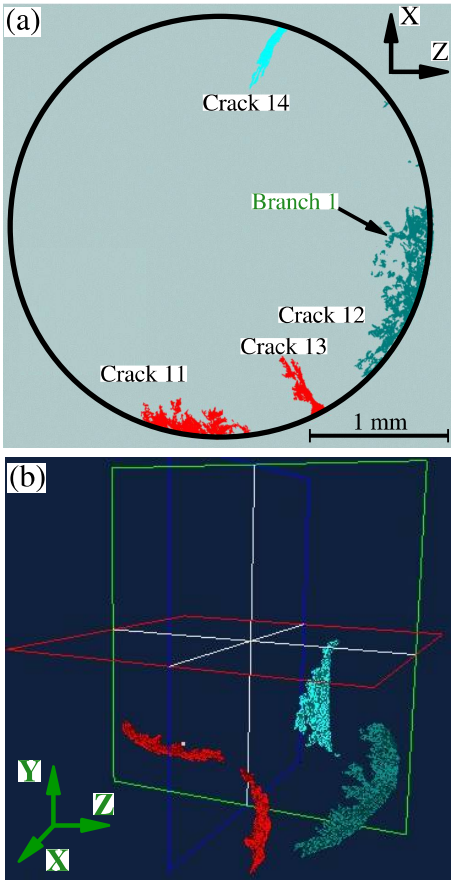

Figure 5: (a) 2D projection along the sample axis of the four cracks present within the pre-cracked specimen after 195,000 cycles. (b) 3D rendering of the cracks at 215,000 cycles.

Starting with the propagation modes, it is observed that at 215,000 cycles Crack 12 doubles its size by propagating in surface mode II (Fig. 6a). Propagation towards the interior occurs in 45° mode I and is relatively slower compared to the mode II surface growth, leading to a shallow subsurface crack (strip). At 265,000 cycles, two more mode I branches are detected at the internal crack-front while mode II propagation is arrested (Fig. 6b). At the moment when the experiment was concluded (305,000 cycles), five independent mode I branches are observed along the crack front (Fig. 6c) and mode II propagation no longer develops.

Another remarkable feature that is possible to observe with the tomographic images is the opening and closing of the crack flanks during the positive and negative reversals of the remote torque (M_t, see Fig. 7a). At 195,000 cycles, only half of the subsurface strip crack (named as Crack 12 in Fig. 5a and highlighted in blue in Fig. 7b) is distinguishable in the negative reversal, while the branches are almost indistinguishable in both the negative an positive

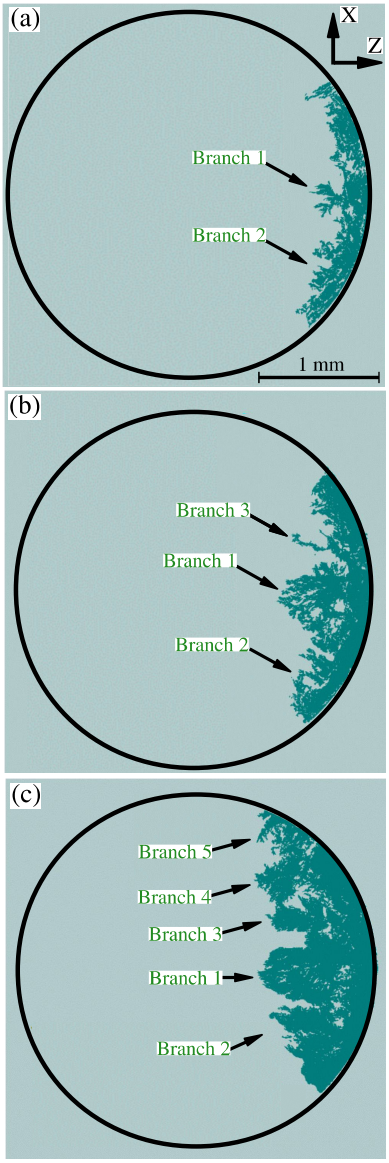

Figure 6: (a) Crack 12 surface projection (following Z axis) at 215,000 cycles, (b) 265,000 cycles, and (c) 305,000 cycles.

reversals (highlighted in orange). Note that this images are obtained by projecting the reconstructed tomographic slices along the Y-axis (using the plugging *Z Project* available on the FIJI™ software [24]). At 215,000 cycles, only the subsurface strip crack is clearly visible during the negative reversal, while both the strip and the branches are visible in the positive reversal (Fig. 7c). Finally, at 265,000 cycles the strip and branches are visible in both the negative and positive reversals, although the crack features are more noticeable in the positive reversal. Therefore, the possibility to observe the crack flanks during the negative reversal increases with the crack size, principally due to the effect of an increasing a length (Fig. 7d). This is most likely induced by a diminishing crack-closure effect due to the increased

roughness of the crack flanks and geometrical mismatches, as shown in Fig. 7e,f. To the best of the authors' knowledge, this is the first time that direct observations of crack opening/closure in torsion resulting from the influence of the σ_1 component are reported in the literature.

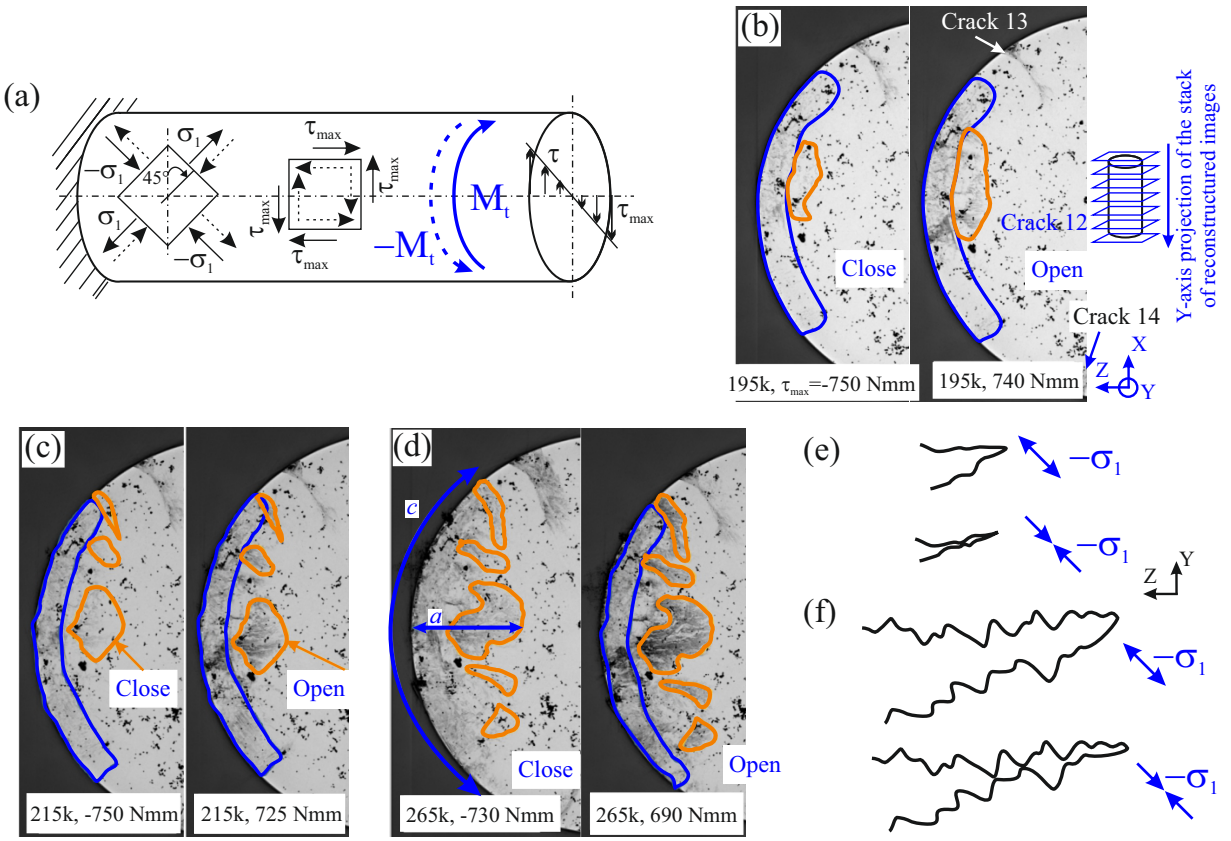

Figure 7: (a) Schematic illustration of τ gradient along the radius, as well as the positive (M_t) and negative (-M_t) reversals of the remote torque with the corresponding τ_{max} and σ_1 components. Projected tomographic images showing the crack-front for (b) the propagation stage at -750 Nmm (left) and 740 Nmm (right) after 195,000 cycles, (c) the propagation stage at -750 Nmm (left) and 725 Nmm (right) after 215,000 cycles, and (d) the propagation stage at -730 Nmm (left) and 740 Nmm (right) after 265,000 cycles. Schematic illustration of the crack flanks displacement for (e) the case of an early-stage mode I crack and (f) the case of a mode I crack at and advanced stage.

Regarding crack morphology, Fig. 8 shows measurements of a depth and c surface crack lengths against the number of cycles (N). At 195,000 cycles, the a/c ratio is 0.33 and decreases to 0.25 at 215,000 cycles. At this point the crack exhibits a characteristic strip shape with a long crack length at the surface and very limited depth. From this point on, a depth and c surface crack lengths exhibit similar slopes until the last measurement taken at 285,000 cycles.

3.3.2. Longitudinal cuts on secondary cracks

The multiple secondary cracks present in the post-mortem macroscopic specimen offer the opportunity to study the influence of grain orientation on the inward crack growth. To do so, some of the specimens were sectioned across the longitudinal direction. This approach has, however, the limitation of not knowing if the grain located at the surface

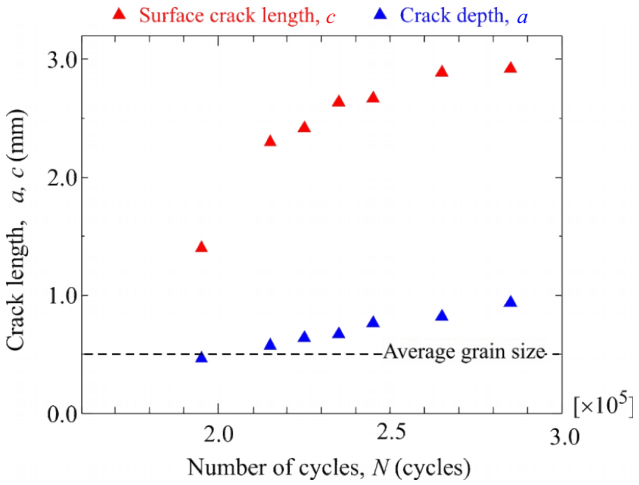

Figure 8: Graph of the a depth and c surface crack length measurements against the number of cycles N.

(in this case Grain 21 in Fig. 9b) is the nucleating one.

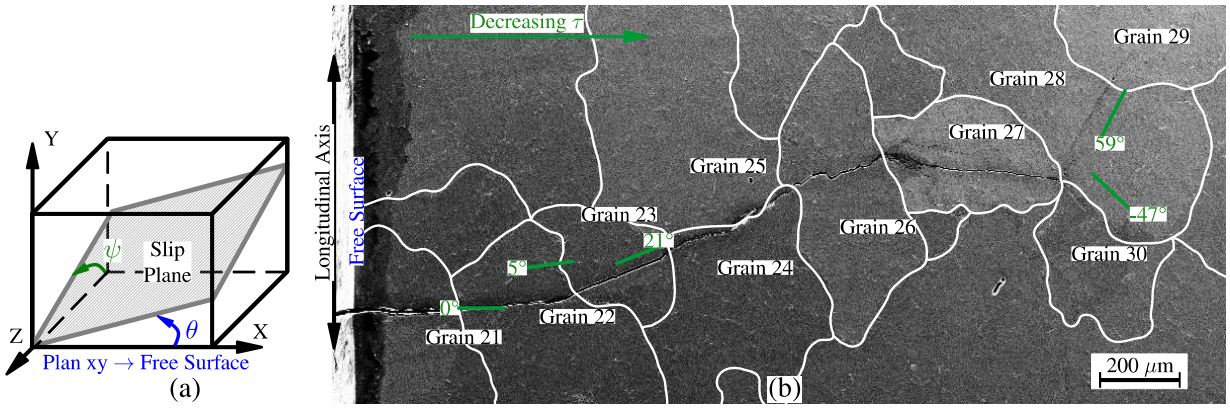

Figure 9: (a) Schematic illustration of a torsional slip plane where the θ angle corresponds to crack orientation at the intersection with the free surface and the ψ angle to the intersection with a longitudinal cut. (b) SEM image at low magnification of a secondary crack observed in a post-mortem specimen cycled at τ_{max} = 90 MPa. EBSD grain boundaries are outlined in white.

Fig. 9a is a schematic illustration of the ψ angle used to measure inward crack orientation. Fig. 9b shows a secondary crack that propagated at τ_{max} = 90 MPa, where the grain boundaries are outlined in white. EBSD results indicate that inward propagation through the three first grains (*i.e.,* Grain 21, Grain 22 and Grain 23) followed crystallographic planes. Afterwards, the crack propagation seems to occur in mode I trough Grain 24, Grain 26 and Grain 27. Finally, the crack encounters a triple point at the end of Grain 27, from where it bifurcates, also following propagation in mode I. Because crack growth through Grain 28 and Grain 30 follows different directions, mode I propagation seems also to be influenced by the underlying crystal orientation. This would mean that, for the crack length and stress level studied, and regardless of the propagation mode, the propagation remains influenced by the underlying crystal orientation through all the crack length.

4. Discussion

In fine grain alloys (*i.e.,* average grain size between 5 and 50 µm) the transition from mixed mode II-mode III to mode I occurs when ΔK_{II} cannot exceed $\Delta K_{II,th}$[2] due to a sustained increasing friction between crack flanks as a result of crack growth (*i.e.,* shear closure [14]). Since $\Delta K_{I,th}$ is smaller than $\Delta K_{II,th}$, once the mode I propagation is set, cracks are still locally influenced by the mode II stress field and therefore propagate on planes located at ±70.5° planes, which is in agreement with the stress distribution of the maximum tangential normal stress ahead of the crack tip [33, 34]. When the crack has sufficiently grown to be no longer affected by this singular stress distribution, the mode I propagation continues at ±45° planes that correspond to the torsional remote stress field. Compared to this situation, the material studied here contains much larger grains. This induces two main differences: (i) a strong influence of grain orientation on crack initiation can be observed, and (ii) the propagation, even for cracks with a millimetric size, is still influenced by the underlying grain structure (especially when the stress level is low), which leads to mode I branches propagating at angles other than ±45° or ±70.5°, as shown in Fig. 9.

4.1. Mechanisms controlling crack initiation

Fig. 10a-b shows an EBSD map with the Taylor factor M values of each grain. A large Taylor factor indicates that a large amount of slip is necessary to accommodate a prescribed increment in plastic strain in a specific grain. None of the nucleating grains have the lowest Taylor factor values (~2, corresponding, for example, to Grain 12 or Grain 14). Moreover, the value of Grain 5 is one of the highest (~3.9). Since the nucleating cracks show distinctive crystallographic features, it seems, therefore, more appropriate to examine the shear rate of each slip plane.

The normalized shear rates, $\dot{\gamma}^s/D^p_{eq}$, are shown in Fig. 10c for the different grains. It results that most of the planes nucleating cracks (shown in red) are those with the highest absolute shear rates. Grain 8 is the exception to this condition, which is most likely explained by the influence of the φ angle (see Fig. 10b). The nucleating $(11\bar{1})[\bar{1}10]$ slip system has a φ = -2° and an absolute shear rate of 0.86, while the direction with the highest absolute shear rate ($(\bar{1}11)[0\bar{1}1]$ and 1.15) has a φ = -40°. This significant difference in φ angles would compensate for a smaller difference in absolute shear rates. Also note that both θ and ψ angles of the nucleating planes are relatively low (*i.e.,* close to 0°), which indicates that, as expected, cracks tend to initiate on planes almost perpendicular to the Y-direction. As shown in Fig. 5, given the sufficient conditions, cracks also can nucleate in planes with orientations closely parallel to the Y-direction. It is remarkable that the reason why Crack 1 propagated through Grain 1 and Grain 2, without apparent deflection at the surface, is because they share slip planes that are almost parallel. Moreover, the analysis of the φ

[2]The fatigue crack growth threshold ΔK_{th} is defined as the ΔK value at which the fatigue crack growth rate da/dN of long cracks approaches zero.

angles indicates that the initiation of Crack 1 likely occurred at Grain 1 and then readily propagated to Grain 2. This is because the φ of the direction with the highest absolute shear rate (0.99 in $(11\bar{1})[011]$ slip system) is -43°in Grain 2, while the $(11\bar{1})[\bar{1}10]$ slip system (which is the most active in Grain 1, where φ = 8°) has an absolute shear rate of 0.45 and a φ angle of -16°.

In summary, Fig. 10c shows that all grains containing a crack have (predicted) plastic activities which are among the highest values ($|\dot{\gamma}^s|/D^p_{eq} \approx 1$) of all the grains analysed, and the planes are favourably oriented with low values of θ, ϕ and φ. However, there are some exceptions like, for example, Grain 13. Thus, if all, those conditions may be necessary to initiate a crack but they may not be sufficient. It must be noted that the Taylor approach [35] is a simplified representation of the mechanics of polycrystals deformation. This approach considers that the strain is uniform throughout the aggregate and fails to take into account the way grains interact with their surroundings. Hence, the most likely additional condition influencing crack initiation would be the local stress state resulting from the mismatch between grains. 2D Image-based crystal plasticity Finite Element (FE) modelling would be required to confirm this point. However, even this modelling could be insufficient, as it does not account for the 3D grain interactions below the surface [36].

Note that it has been reported that a flattened zone of this size has a considerable influence on stress gradient within the gauge volume [17]. Moreover, the corners between the flattened zone and the cylinder perimeter can act as local stress raisers. The cracks shown in Fig. 10a nucleated away from the corners, and therefore, it is considered that their initiation is not driven by a stress concentration effect induced by the corners.

4.2. Mechanisms controlling crack propagation

As far as the authors are aware, direct images of fatigue cracks growing in torsion have only been obtained by D.Shiozawa et al [37] in a Ti alloy (ex situ observations, no load applied). In this work, which also employed synchrotron tomography, stress intensity factor (SIF) values were calculated from analytical formulas in order to explain crack branching. Regarding the results reported in the present work, it was shown that, in their early stage of propagation, fatigue cracks were relatively shallow with a very planar surface (corresponding to a highly activated slip plane) and a constant depth a of the order of ~200 μm. To the authors knowledge, this peculiar crack development have never been reported in the literature for torsion cracks. It could be related to the evolution of the stress gradient across the sample diameter. To check this assumption, a FE analysis based on the experimentally observed shape of Crack 12 has been carried out to calculate the SIF along the crack front. The FE approach was chosen in spite of its complexity with respect to analytical formulas because of the difficulty of accurately taking into account both the evolving crack size and shape, as well as the decreasing shear stress level.

(a)

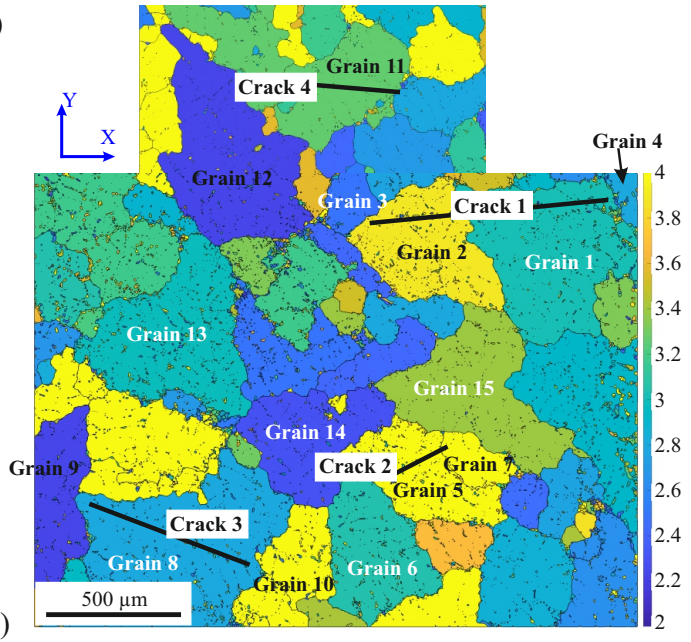

(b)

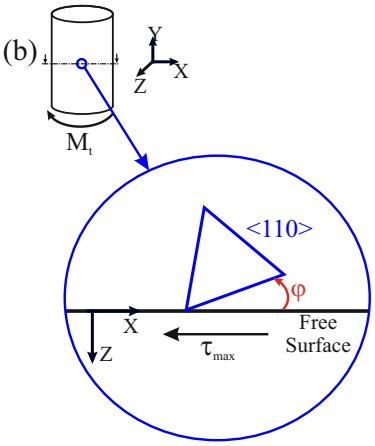

(c)

	(111) [0$\bar{1}$1]	(111) [10$\bar{1}$]	(111) [$\bar{1}$10]	($\bar{1}$11) [01$\bar{1}$]	($\bar{1}$11) [101]	($\bar{1}$11) [110]	(1$\bar{1}$1) [011]	(1$\bar{1}$1) [10$\bar{1}$]	(1$\bar{1}$1) [110]	(11$\bar{1}$) [011]	(11$\bar{1}$) [101]	(11$\bar{1}$) [$\bar{1}$10]	Size (mm^2)
Grain 1	θ = 63°; ψ = 84°			θ = -55°; ψ = -23°			θ = 69°; ψ = -61°			**θ = 12°; ψ = 12°; (φ = 8°)**			0.28
	0	-0.57	0.16	0	0	0	-0.01	0.81	0	-0.08	0	-1.23	Crack
Grain 2	θ = 39°; ψ = -64°			θ = -61°; ψ = 32°			θ = 82°; ψ = 82°			**θ = 11°; ψ = 9°; (φ = -43°)**			0.17
	0.13	-0.11	0	0	0	0	0	0.97	0.06	-0.99	0	-0.45	Crack
Grain 5	θ = -67°; ψ = -76°			θ = 51°; ψ = -52°			**θ = 20°; ψ = 27°**; (φ = 32°)			θ = -54°; ψ = 20°			0.11
	-0.98	0.36	0	0.48	0.27	0	0.09	-1.11	0	0.20	0.08	0	Crack
Grain 8	θ = -6°; ψ = -79°			θ = 81°; ψ = 70°; (φ = -40°)			θ = 47°; ψ =36 °			**θ = -17°; ψ = -9°; (φ = -2°)**			0.37
	-0.44	0.01	0	1.15	0	-0.06	0	0	0	0	0.09	-0.86	Crack
Grain 11	θ = -86°; ψ = -87°			**θ = -7°; ψ = -16°**; (φ = 23°)			θ = -49°; ψ = 54°			θ = 64°; ψ = -7°			0.16
	0	-0.72	0	-1.05	0	0.14	0	0	0	0	-0.10	0.02	Crack
Grain 12	θ = 46°; ψ = -70°			**θ = 26°; ψ = 49°; (φ= -6 °)**			**θ = -21°; ψ = -11°**			θ = 89°; ψ = -14°			0.26
	0.11	0	0	-0.07	0	0	0	0	0	0	-0.63	1.31	No Crack
Grain 13	θ = -55°; ψ = -77°			θ = 46°; ψ = 34°			**θ = 2°; ψ = -32°; (φ = -14°)**			θ = -65°; ψ =-3°			0.25
	-0.27	0.52	0	0	0	0	0	-1.66	-0.05	0.39	0	0.07	No Crack
Grain 14	θ = 41°; ψ = 64°			θ = 39°; ψ = -59°			**θ = -15°; ψ = 2°; (φ = 29°)**			θ = -85°; ψ = -19°			0.16
	0	0	0	0	0	0	0	-0.31	-0.21	0	-0.68	0.90	No Crack
Grain 15	θ = 59°; ψ = 77°			**θ = -26°; ψ = -26°; (φ = 22°)**			θ = -66°; ψ = 61°			θ = 45°; ψ = -5°			0.23
	0.54	-0.80	0	-0.91	-0.11	0	-0.16	0.93	0	-0.09	-0.09	0	No Crack

Figure 10: (a) EBSD map (same as in Fig. 4c) showing the Taylor factor M values of each grain. (b) Schematic illustration of φ angle between the free surface and a slip system, with the <110> directions shown in blue. (c) Table containing the normalized shear rates, $\dot{\gamma}^s/D^p_{eq}$, of the grains labelled in (a). The angles in red refer to planes where the cracks were nucleated, whereas the angles in blue correspond to planes with the lowest absolute θ values for some large grains that did not nucleate any crack. The φ angle in parenthesis correspond to the slip system with the highest slip activity within the corresponding {111} plane.

The geometrical model used to describe the curved crack fronts was generated using the GMSH™ [38] free-software. The model is subsequently adapted to match the crack size observed in the tomographic images (see Fig. 11a). The a_{II} value is kept constant (250 μm) while the c surface length is regularly increased. The mesh consists of three zones, with fine elements for both the crack lips and the crack tip, while a coarser mesh is used in the rest of the gauge (D = 3 mm). In this last region, a distance map specifying the size of the elements according to the distance to the crack front is applied. The whole mesh is made of brick elements. The remote torque T = 650 N·mm (equivalent to τ = 120 MPa) is applied on the top surface of a cylinder representative of the gauge volume, where the movement in Z and Y directions is fixed. The cylinder base has the three displacement degrees of freedom constrained. The material is considered as a linear isotropic solid. The interaction integral method provided by Abaqus™ is used to extract the stress intensity factors directly from the crack front. An example of the calculated mode I, mode II and mode III SIF values for a given crack length is shown in Fig. 11b. Note that K_I is equal to zero along all crack front. The absolute value of K_{II} is maximal at the two intersections with the free surface. Finally, K_{III} is maximal at the centre of the crack front.

The simulation results (Fig. 11c) for the various development stages of Crack 12 indicate that, even when mode II is dominant for small crack sizes, there is a turning point at approximately c = 1.5 mm where the maximal K_{III} values overtake the K_{II} ones. Tomographic images show that Crack 12 mode II surface propagation is halted at $c \approx 2.3$ mm.

At that stage, one could expect the crack to grow towards the interior of the sample under the influence of mode III loading as a result of the value of K_{III} becoming higher than a (hypothetical) K_{II} threshold. However, very little is known on such thresholds in the literature, as they are experimentally very difficult to measure. In the case of Crack 12, 3D observations show, however, a different mechanism: several independent branches inclined at planes closer to 45° are observed, indicating a change into mode I growth (Fig. 6). As explained at the beginning of the discussion, this change of crack growth mode stems from the increasing surface contact between the crack flanks, which leads to an increase in friction (i.e., shear closure) and, consequently, to the reduction of the driving force acting on a mode II-mode III crack. Studies on the formation of factory roof morphologies indicate that mode I branches form at specific sites over the semi-elliptical crack front. This sites correspond to locations where the $K_{I,eff}$ value of a yet-to-be-formed branch would be maximal [34, 39, 40]. At this stage, the onset of mode I branches occurs when the mode II-mode III driving force diminishes to a value smaller than the ΔK_I expected at the plane of the yet-to-be-formed branch. In addition, the branching will only occur if this ΔK_I is higher that the ΔK_{Ith} related to the applied cyclic ratio and environmental conditions [14, 40]. Note that the location of the maximal $K_{I,eff}$ varies with the aspect ratio a/c of the crack-front [39]. Also, another significant difference between the literature and the current study, apart from the grain size, is that fracture surfaces observed in Zone 2 do not exhibit the characteristic factory-roof features, which are

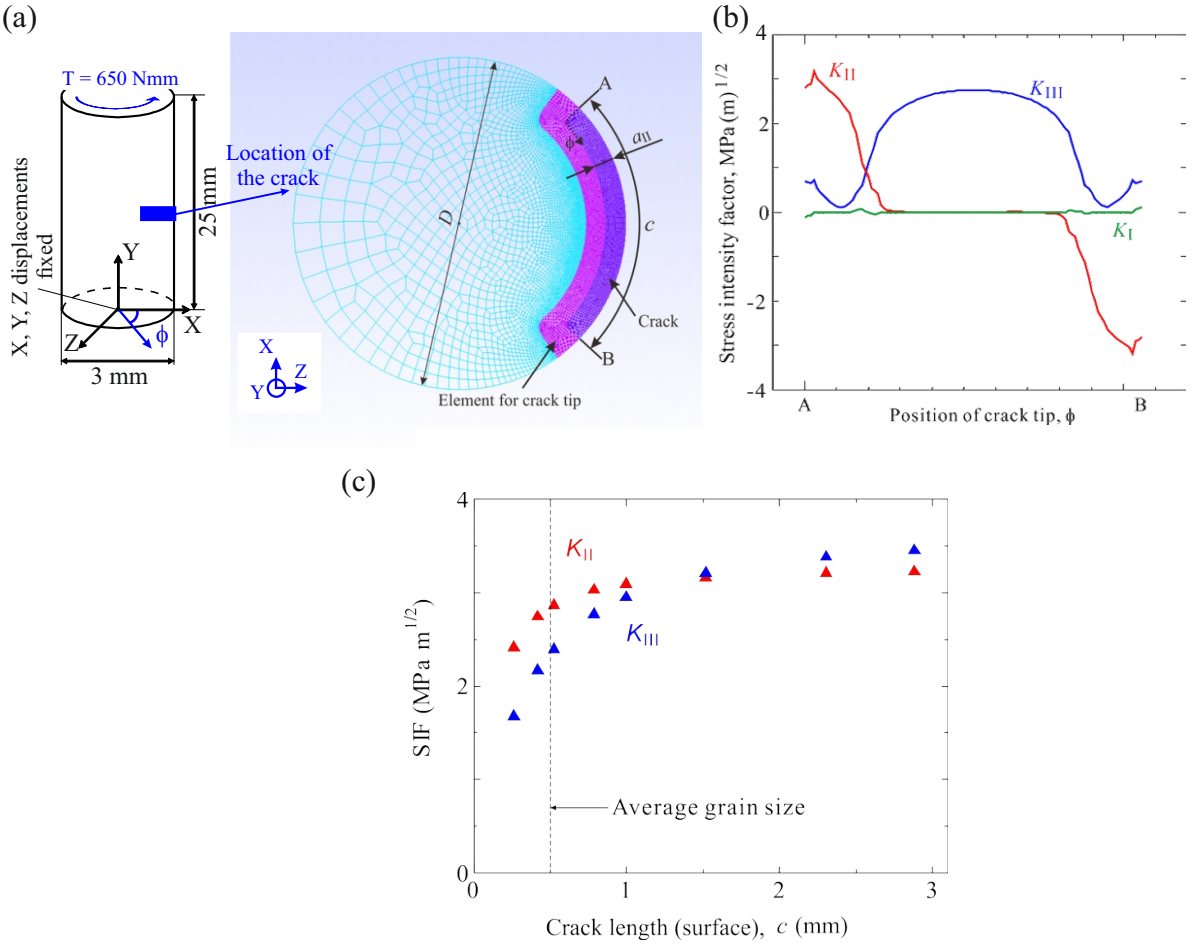

Figure 11: (a) Cross section of one of the meshes used for the calculation of SIF with the crack lips in violet and the crack tip in magenta. (b) Plot of mode I, mode II and mode III stress intensity values calculated along the crack tip, ϕ. The displayed results correspond to a crack of a_{II} = 250 μm and c = 750 μm undergoing a remote load of T = 650 Nmm (τ = 120 MPa). (c) Plot of the mode II and mode III maximum SIF results against the c surface crack length.

observed in V-notched fatigue specimens, but more rarely in smooth fatigue specimens, such as the ones studied here.

Nevertheless, the explanation for the mechanisms controlling mode I transition appears controversial in the literature. On one side, a mechanistic model has been proposed, which assumes that macroscopic mode III occurs as a result of microscopically alternating mode II propagation [41, 42]. According to this model, crack propagation entirely occurs in mode II before switching into mode I, and the critical ΔK_I-value necessary for branching would be approximately 20% higher than the maximum $K_{II}/2$-value developing at the crack front. Taken from Fig. 11b, $K_{II}/2$ =1.2 MPa m$^{1/2}$ and so, the related critical K_I is 1.44 MPa m$^{1/2}$, which is significantly higher than the $\Delta K_{eff,th} \approx 0.9$ MPa m$^{1/2}$ reported for aluminium alloys [43].

So the mechanisms described in [41, 42] might be active in our case, at least in Zone II of the fatigue curve (Fig. 3), where the size of the crap-tip plastic zone is assumed to be smaller than the grain size. In that case, the mixed

mode II-mode III crack growth would be influenced by the slip planes within the different grains. However, the flat fracture surfaces observed in Zone 1 (Fig. 3a) also suggest a change in the mechanisms at play for higher stress levels. In Zone 1, the mode III stress level can be considered high enough for cracks to be able to propagate in macroscopic mode III, localising the propagation on mechanically-driven macroscopic planes which encompass numerous grains, as proposed in some other works [34, 44, 45]. At that stage, it is quite hard to come to a definitive conclusion and further 3D observations (*e.g.,* by investigating various stress levels while knowing the exact shape and orientation of te grains where crack initiation and propagation take place, which can be achievable by combining phase contrast and diffraction contrast tomography) are needed to elucidate the validity of the mechanisms introduced in this and the preceding paragraphs.

Along the same lines, another puzzling result regarding mixed mode II-mode III propagation is the fact that flat fracture surfaces are expected for the stress level investigated at the synchrotron ($\tau_{max} > 100$ MPa, see in section 3.1,). As the sample containing Crack 12 has not been cycled to fracture, one does not know if the final failure would have occurred from that particular crack, leading to a Zone 2 fracture surface or from another of the cracks detected in the sample gauge length, which might have lead to a Zone 1 flat fracture surface. Another possible explanation to this difference in behaviour between macroscopic and tomography specimens is the microstructural influence. The macroscopic specimens were machined out of the centre of the original rods (see section 2), while the tomography specimens were carved out at a location that is close to the rod's free surface. Therefore, the average values of SDAS and grain size could be smaller in the tomography specimens, which would increase the material resistance to crack propagation [17] and lead to a hypothetical Zone 1-to-Zone 2 shift in fracture surface morphology.

Fig. 12 summarizes the main stages of the torsional crack initiation and propagation behaviour observed in this study. First, it is considered that the ability of a crack to rapidly grow in mode II and form a strip-like crack seems to depend on preferably oriented surface grains (Fig. 12a), which lay between neighbours sharing slip planes with relatively low misalignment, as shown in Fig. 10c.

It is assumed that even if the crystal orientation is favourable along the perimeter, there is a moment where the inward propagation will switch into mode I (Fig. 12c). However, the role of grain boundaries on the switching into mode I is unclear. It could be postulated that the switch is purely induced by the (hypothetical) K_{II} threshold (see Fig. 12b). This means that the switching can occur at any position within the grains at the surface. As it was observed that cracks tend to deflect at grain boundaries (Fig. 9b), another possibility is that, once the crack size is approaching the K_{II} threshold, the grain boundaries will act as starting points for the branching (Fig. 12c). A detailed investigation on the effect of grain boundaries is complicated, especially in the case where a large distribution of grain size is observed, such as in the studied material. To further elucidate this issue, synchrotron in situ testing could be combined

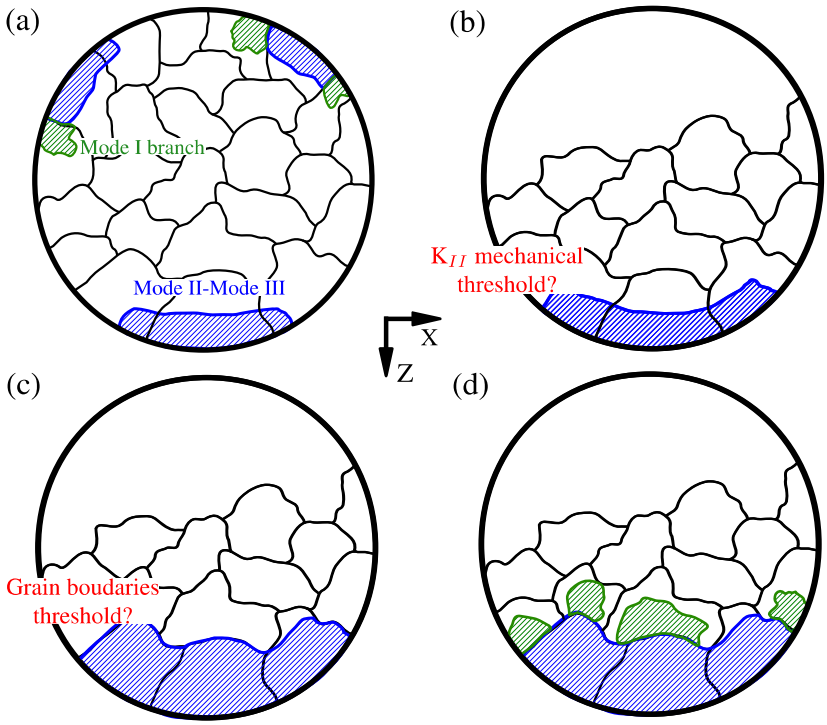

Figure 12: Summary of the crack growth stages in Zone 2 according to the synchrotron observations: (a) early stages of the propagation period; (b) the possibility of a K_{II} threshold; (c) or a threshold induced by grain boundaries and (d) crack propagation after branching occurs.

with Diffraction Contrast Tomography (DCT), or even EBSD serial sectioning after the synchrotron in situ testing.

The main part of the inward propagation develops in mode I (Fig. 12c). As shown in Fig. 9b, the angle of the branches seems to be influenced by the underlying microstructure. Moreover, regardless of a K_{II} or grain boundary threshold, the crack branches are formed at different moments of the propagation (Fig. 6). This is probably due to the mode II-mode I α crack-plane twisting. It has been reported that the resistance to twisting varies depending on the α misorientation: the higher the area to be fractured by the crack, the higher the branching retardation will be [46, 47].

Finally, because the tomographic images were obtained under load, it can be seen (qualitatively) that the strong geometrical deviations resulting from the mode I crack branches in the bulk considerably disrupt the crack closure/opening behaviour. Such closure mechanisms, seemingly caused by the roughness of the crack surface, result in the inclined parts of the crack never being able to completely close, even when the sign of the normal stress acting on it changes. This suggests an acceleration of crack growth (assuming that a closed crack would not propagate in mode I), which is not predicted by the few models which have tried to address this issue (*e.g.,* [48]). Further observations at higher resolution are therefore required to be more quantitative on this point.

5. Conclusions

The combination of techniques such as EBSD analysis and synchrotron in situ testing enabled the investigation of the mechanisms controlling crack initiation and propagation under torsional loading for an A357-T6 cast alloy. The conclusions are as follows:

1. Depending on the stress level, three different types of fractographic morphologies are observed.
2. Favourable crystallographic orientations control the initiation period where several cracks can be simultaneously formed (multi-cracking).
3. Newly initiated cracks are prone to grow in mode II over the free surface while inward propagation is rapidly arrested. This behaviour leads to shallow cracks with a low a/c ratio (0.33-0.25). This observation has never been reported before.
4. Surface mode II propagation is arrested when the c surface crack length is long enough to induce comparatively higher mode III driving forces. At this point, however, surface cracks tend to switch into mode I growth and mode III is not observed.
5. Inward propagation continues by branching into mode I. The branching seems to be most certainly influenced by the crystallography.
6. At intermediate-low stress levels, grains boundaries are responsible for crack deflections and bifurcations at the surface, as well as in the bulk of the samples.

Acknowledgments

The French National Research Agency (ANR) is thanked for the funding of this project: "Influence des DEfauts de Fonderie sur la Fatigue des Alliages Aéronautiques" (IDEFFAAR ANR-10-RMNP-0016). Gratitude is also expressed to the local contacts at ID19 beamline (ESRF) for they collaboration during the experiments.

References

[1] J. Ødegård, K. Pedersen, Fatigue Properties of an A356 (AlSi7Mg) Aluminium Alloy for Automotive Applications - Fatigue Life Prediction, SAE IntTechnical Paper 940811 (1994). doi:10.4271/940811.

[2] S. Stanzl-Tschegg, H. Mayer, A. Beste, S. Kroll, Fatigue and fatigue crack propagation in AlSi7Mg cast alloys under in-service loading conditions, Int J Fatigue 17 (2) (1995) 149–155. doi:http://dx.doi.org/10.1016/0142-1123(95)95895-N.

[3] J.-Y. Buffiere, S. Savelli, P. Jouneau, E. Maire, R. Fougeres, Experimental study of porosity and its relation to fatigue mechanisms of model Al-Si7-Mg0.3 cast Al alloys, Mat Sci Eng A 316 (1-2) (2001) 115–126. doi:10.1016/S0921-5093(01)01225-4.

[4] G. Pluvinage, Fracture and Fatigue Emanating from Stress Concentrators, Springer, 2003.

[5] Y. X. Gao, J. Z. Yi, P. D. Lee, T. C. Lindley, The effect of porosity on the fatigue life of cast aluminium-silicon alloys, FFEMS 27 (7) (2004) 559–570. doi:10.1111/j.1460-2695.2004.00780.x.

[6] Q. Wang, P. Crepeau, C. Davidson, J. Griffiths, Oxide films, pores and the fatigue lives of cast aluminum alloys, Metall Mater Trans B 37 (6) (2006) 887–895. doi:10.1007/BF02735010.

[7] H. Ammar, A. Samuel, F. Samuel, Effect of casting imperfections on the fatigue life of 319-F and A356-T6 Al-Si casting alloys, Mat Sci Eng A 473 (1-2) (2008) 65–75. doi:10.1016/j.msea.2007.03.112.

[8] X. Zhu, J. Jones, J. Allison, Effect of Frequency, Environment, and Temperature on Fatigue Behavior of E319 Cast Aluminum Alloy: Stress-Controlled Fatigue Life Response, Metall Mater Trans A 39 (11) (2008) 2681–2688. doi:10.1007/s11661-008-9631-1.

[9] M. Brochu, Y. Verreman, F. Ajersch, D. Bouchard, High cycle fatigue strength of permanent mold and rheocast aluminum 357 alloy, Int J Fatigue 32 (8) (2010) 1233–1242. doi:10.1016/j.ijfatigue.2010.01.001.

[10] L. Zeng, J. Sakamoto, A. Fujii, H. Noguchi, Role of eutectic silicon particles in fatigue crack initiation and propagation and fatigue strength characteristics of cast aluminum alloy A356, Eng Fract Mech 115 (0) (2014) 1–12. doi:http://dx.doi.org/10.1016/j.engfracmech.2013.11.016.

[11] S. Suresh, Fatigue of Materials (1998). doi:https://doi.org/10.1017/CBO9780511806575.

[12] E. Tschegg, A contribution to mode III fatigue crack propagation, Mat Sci Eng 54 (1) (1982) 127–136. doi:http://dx.doi.org/10.1016/0025-5416(82)90037-4.

[13] E. K. Tschegg, Mode III and mode I fatigue crack propagation behaviour under torsional loading, J Mater Sci 18 (6) (1983) 1604–1614. doi:https://doi.org/10.1007/BF00542053.

[14] E. Tschegg, R. Ritchie, F. McClintock, On the influence of rubbing fracture surfaces on fatigue crack propagation in mode III, Int J Fatigue 5 (1) (1983) 29–35. doi:http://dx.doi.org/10.1016/0142-1123(83)90005-1.

[15] J. Schijve, Fatigue of Structures and Materials (2009). doi:10.1007/978-1-4020-6808-9.

[16] D. Socie, Critical Plane Approaches for Multiaxial Fatigue Damage Assessment, West Conshohocken, PA: ASTM International, 1993, pp. 7–36. doi:doi:https://doi.org/10.1520/STP24793S.

[17] G.-C. Le, F. Morel, D. Bellett, N. Saintier, P. Osmond, Multiaxial high cycle fatigue damage mechanisms associated with the different microstructural heterogeneities of cast aluminium alloys, Mat Sci Eng A 649 (2016) 426–440. doi:http://dx.doi.org/10.1016/j.msea.2015.10.026.

[18] M. I. Houria, Y. Nadot, R. Fathallah, M. Roy, D. M. Maijer, Influence of casting defect and SDAS on the multiaxial fatigue behaviour of A356-T6 alloy including mean stress effect, Int J Fatigue 80 (2015) 90–102. doi:http://dx.doi.org/10.1016/j.ijfatigue.2015.05.012.

[19] I. Koutiri, D. Bellett, F. Morel, L. Augustins, J. Adrien, High cycle fatigue damage mechanisms in cast aluminium subject to complex loads, Int J Fatigue 47 (0) (2013) 44–57. doi:10.1016/j.ijfatigue.2012.07.008.

[20] M. Roy, Y. Nadot, D. M. Maijer, G. Benoit, Multiaxial fatigue behaviour of A356-T6, FFEMS 35 (12) (2012) 1148–1159. doi:10.1111/j.1460-2695.2012.01702.x.

[21] I. Serrano-Munoz, Influence of casting defects on the fatigue behaviour of an A357-T6 aerospace alloy (2014). URL http://theses.insa-lyon.fr/publication/2014ISAL0117/these.pdf

[22] ISO-1352-2011, Metallic Materials – Torque-controlled fatigue testing. International Standard (2011).

[23] ESRF (Accessed 2017). [link].

URL http://www.esrf.eu/UsersAndScience/Experiments/Imaging/ID19

[24] J. Schindelin, I. Arganda-Carreras, E. Frise, V. Kaynig, M. Longair, T. Pietzsch, S. Preibisch, C. Rueden, S. Saalfeld, B. Schmid, J.-Y. Tinevez, D. J. White, V. Hartenstein, K. Eliceiri, P. Tomancak, A. Cardona, Fiji: an open-source platform for biological-image analysis, Nat Methods 9 (2012) 676 EP –, perspective.
URL http://dx.doi.org/10.1038/nmeth.2019

[25] O. Instruments, Aztechkl (Last accessed in 2020).
URL https://nano.oxinst.com/products/aztec/aztechkl

[26] P. Van Houtte, S. Li, M. Seefeldt, L. Delannay, Deformation texture prediction: from the Taylor model to the advanced Lamel model, Int J Plast 21 (3) (2005) 589–624. doi:10.1016/j.ijplas.2004.04.011.

[27] L. Delannay, M. Melchior, J. Signorelli, J.-F. Remacle, T. Kuwabara, Influence of grain shape on the planar anisotropy of rolled steel sheets–evaluation of three models, Comput. Mater. Sci. 45 (3) (2009) 739–743. doi:10.1016/j.commatsci.2008.06.013.

[28] S. Dancette, L. Delannay, T. Jodlowski, J. Giovanola, Multisite model prediction of texture induced anisotropy in brass, Int J Mater Form 3 (1) (2010) 251–254. doi:10.1007/s12289-010-0754-8.

[29] S. Dancette, L. Delannay, K. Renard, M. Melchior, P. Jacques, Crystal plasticity modeling of texture development and hardening in TWIP steels, Acta Mater 60 (5) (2012) 2135–2145. doi:10.1016/j.actamat.2012.01.015.

[30] L. Delannay, P. J. Jacques, S. R. Kalidindi, Finite element modeling of crystal plasticity with grains shaped as truncated octahedrons, Int J Plast 22 (10) (2006) 1879–1898. doi:10.1016/j.ijplas.2006.01.008.

[31] S. Dancette, A. Browet, G. Martin, M. Willemet, L. Delannay, Automatic processing of an orientation map into a finite element mesh that conforms to grain boundaries, Modell Simul Mater Sci Eng 24 (5) (2016) 055014. doi:https://iopscience.iop.org/article/10.1088/0965-0393/24/5/055014#back-to-top-target.

[32] R. Hielscher, F. Bartel, T. B. Britton, Gazing at crystal balls: Electron backscatter diffraction pattern analysis and cross correlation on the sphere, Ultramicroscopy 207 (2019) 112836. doi:https://doi.org/10.1016/j.ultramic.2019.112836.

[33] Y. Murakami, S. Hamada, A NEW METHOD FOR THE MEASUREMENT OF MODE II FATIGUE THRESHOLD STRESS INTENSITY FACTOR RANGE ΔKτth, FFMES 20 (6) (1997) 863–870. doi:10.1111/j.1460-2695.1997.tb01530.x.

[34] Y. MURAKAMI, K. TAKAHASHI, R. KUSUMOTO, Threshold and growth mechanism of fatigue cracks under mode II and III loadings, FFMES 26 (6) (2003) 523–531. doi:10.1046/j.1460-2695.2003.00644.x.

[35] G. I. Taylor, Plastic strain in metals, J Inst Met (62) (1938) 307–324.

[36] I. Serrano-Munoz, S. Dancette, C. Verdu, J.-Y. Buffiere, Influence of Pore Size and Crystallography on the Small Crack HCF Behavior of an A357-T6 Cast Aluminum Alloy, Met Mat Trans A 51 (3) (2020) 1416–1427. doi:10.1007/s11661-019-05590-6.
URL https://doi.org/10.1007/s11661-019-05590-6

[37] D. Shiozawa, Y. Nakai, T. Murakami, H. Nosho, Observation of 3D shape and propagation mode transition of fatigue cracks in Ti-6Al-4V under cyclic torsion using CT imaging with ultra-bright synchrotron radiation, Int J Fatigue 58 (2014) 158–165. doi:10.1016/j.ijfatigue.2013.02.018.

[38] C. Geuzaine, J.-F. Remacle, Gmsh: a three-dimensional finite element mesh generator with built-in pre- and post-processing facilities, Int J Numer Methods Eng 79(11) (2009) 1309–1331.
URL https://gmsh.info/doc/preprints/gmsh_paper_preprint.pdf

[39] Y. MURAKAMI, K. TAKAHASHI, K. TOYAMA, Mechanism of crack path morphology and branching from small fatigue cracks under mixed loading, FFMES 28 (1-2) (2005) 49–60. doi:10.1111/j.1460-2695.2004.00828.x.

[40] J. Pokluda, K. Slamecka, P. Sandera, Mechanism of factory-roof formation, Eng Fract Mech 77 (11) (2010) 1763–1771. doi:10.1016/j.

435 engfracmech.2010.03.031.

436 [41] J. Pokluda, R. Pippan, Can pure mode III fatigue loading contribute to crack propagation in metallic materials?, FFEMS 28 (1-2) (2005)
437 179–185. doi:10.1111/j.1460-2695.2004.00843.x.

438 [42] J. Pokluda, G. Trattnig, C. Martinschitz, R. Pippan, Straightforward comparison of fatigue crack growth under modes II and III, Int J Fatigue
439 30 (8) (2008) 1498–1506. doi:10.1016/j.ijfatigue.2007.09.009.

440 [43] R. Pippan, The effective threshold of fatigue crack propagation in aluminium alloys. I. The influence of yield stress and chemical composition,
441 Philos. Mag. A 77 (4) (1998) 861–873. arXiv:https://doi.org/10.1080/01418619808221216, doi:10.1080/01418619808221216.

442 [44] S. Beretta, G. Donzella, R. Roberti, A. Ghindini, Contact Fatigue propagation of deep defects in rail way wheels, in: Proc. 13th European
443 Conference on Fracture, ECF13, 3R, 2000, p. 147.

444 [45] Y. Murakami, Metal Fatigue: Effects of Small Defects and Nonmetallic Inclusions. Chapter 19: Fatigue threshold in Mode II and Mode III,
445 ΔK_{IIth} and ΔK_{IIIth} and small crack problems. p. 485 (2019).

446 [46] T. Zhai, A. Wilkinson, J. Martin, A crystallographic mechanism for fatigue crack propagation through grain boundaries, Acta Mater 48 (20)
447 (2000) 4917–4927. doi:10.1016/S1359-6454(00)00214-7.

448 [47] W. Ludwig, J.-Y. Buffiere, S. Savelli, P. Cloetens, Study of the interaction of a short fatigue crack with grain boundaries in a cast Al alloy
449 using X-ray microtomography, Acta Mater 51 (3) (2003) 585 – 598. doi:https://doi.org/10.1016/S1359-6454(02)00320-8.

450 [48] J. Tong, R. B. Yates, M. Brown, A model for sliding mode crack closure part I: Theory for pure mode II loading, Eng Fract Mech 52 (4)
451 (1995) 599 – 611. doi:https://doi.org/10.1016/0013-7944(95)00044-V.

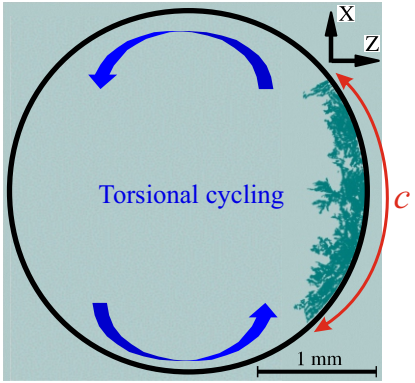

Surface mode II crack propagation

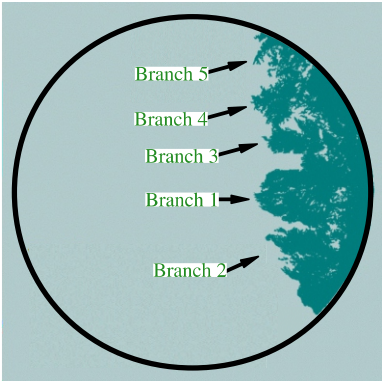

Branches of internal mode I propagation

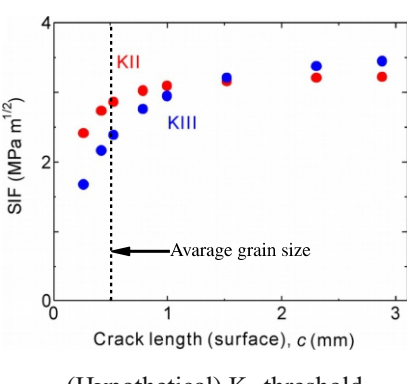

(Hypothetical) K_{II} threshold prior to mode I branching